Available online at www.sciencedirect.com
SCIENCE DIRECT®
Chemical Physics Letters 374 (2003) 235–242
CHEMICAL PHYSICS LETTERS
www.elsevier.com/locate/cplett

Fast beam studies of I_2^- and $I_2^- \cdot Ar$ photodissociation

Alexandra A. Hoops, Jason R. Gascooke, Ann Elise Faulhaber,
Kathryn E. Kautzman, Daniel M. Neumark *

Department of Chemistry, University of California, Berkeley, CA 94720-1460, USA
Chemical Sciences Division, Lawrence Berkeley National Laboratories, Berkeley, CA 94720, USA

Received 6 March 2003; in final form 21 April 2003

Abstract

The photodissociation dynamics of bare I_2^- and $I_2^- \cdot Ar$ at 413 and 390 nm have been investigated using a fast beam instrument coupled with a new photofragment coincidence imaging detector. Results from the application of this technique to the dissociation of I_2^- and $I_2^- \cdot Ar$ yielded the dissociation energy of I_2^- ($D_0(I_2^-) = 1.012 \pm 0.008$ eV) and I_2^-–Ar binding energy ($D_0(I_2^-\text{–Ar}) = 45 \pm 8$ meV). The experiments show that at these wavelengths, $I_2^- \cdot Ar$ undergoes three-body dissociation to $I^- + I^* + Ar$, with very low momentum in the Ar atom and unequal momentum partitioning between the two I atoms.

1. Introduction

Fast beam dissociation experiments coupled with coincident fragment detection represent a powerful method for investigating the fragmentation dynamics of exotic species such as highly excited neutral molecules, reactive free radicals, and mass-selected charged and neutral clusters [1]. In these experiments, a fast charged or neutral molecular beam with several keV of laboratory energy undergoes photodissociation or collision-induced dissociation. The resulting fast fragments are detected directly with high efficiency using a microchannel plate (MCP) detector, and, by measuring the fragments in coincidence, one can extract the product masses, translational energy release, and scattering angle for each dissociation event. The detection schemes originally implemented in these experiments were limited to the measurement of only two fragments per dissociation event [2,3]; such a technique has been used in our laboratory to investigate the photodissociation dynamics of free radicals produced from photodetachment of a fast negative ion beam [4]. In the past few years, several detection systems have been developed to enable coincident detection of three or more fragments from a single dissociation event [5–12], thereby enabling the detailed study of a new class of dissociation phenomena involving multi-body decay [1,13]. We have recently installed a multi-body coincidence imaging detector based on the design of Amitay and Zajfman [6] on our fast beam photodissociation instrument, and here present our first results

---

[*] Corresponding author. Fax: +1-510-642-3635.
E-mail address: dan@radon.cchem.berkeley.edu (D.M. Neumark).

0009-2614/03/$ - see front matter © 2003 Elsevier Science B.V. All rights reserved.
doi:10.1016/S0009-2614(03)00708-5

on the two-body dissociation of I_2^- and three-body dissociation of $I_2^- \cdot Ar$.

Experimental and theoretical studies over the last decade have established bare and clustered I_2^- as model systems for understanding how the photodissociation dynamics of a simple chromophore, I_2^-, are affected by solvation [14]. Time- and frequency-domain experiments have led to a detailed picture of the dissociation dynamics and potential energy surfaces of the bare anion [15–20]. While I_2^- has five low-lying excited electronic states [21,22], the majority of experiments performed have focused on characterizing the X $^2\Sigma^+_{u,1/2}$ and A′ $^2\Pi_{g,1/2}$ states, both of which correlate to $I^- + I\ (^2P_{3/2})$ products [15,16,18,20]. Dissociation from the higher B $^2\Sigma^+_{g,1/2}$ electronic state, which correlates to $I^- + I^*\ (^2P_{1/2})$ products, was investigated by Lineberger and coworkers [17,19]. At the photon energy used to excite the B $^2\Sigma^+_{g,1/2} \leftarrow$ X $^2\Sigma^+_{u,1/2}$ transition, two product channels are energetically accessible:

$$I_2^-\ B\ ^2\Sigma^+_{g,1/2} \rightarrow I^- + I\ (^2P_{3/2}) \qquad \Delta H_{rxn} = 1.007 \pm 0.005\ \text{eV} \tag{1}$$

$$\rightarrow I^- + I^*\ (^2P_{1/2}) \qquad \Delta H_{rxn} = 1.950 \pm 0.005\ \text{eV}, \tag{2}$$

but the measured neutral fragment time-of-flight spectra reveal that only $I^- + I^*\ (^2P_{1/2})$ photofragments are produced. The heats of reaction for processes (1) and (2) are based on the dissociation energy of I_2^- by Zanni et al. [16] and the spin–orbit splitting of the iodine atom.

The addition of solvent molecules to I_2^- significantly affects its dissociation dynamics [14]. For example, the photodissociation of $I_2^- \cdot Ar_n$ ($n = 1$–27) with 790 nm laser light revealed the presence of competing reaction pathways leading to uncaged, caged, and solvent-separated products [23]. For the small cluster $I_2^- \cdot Ar$, the only charged product observed was I^-, implying the existence of three-body dissociation to $I^- + I\ (^2P_{3/2}) + Ar$. At higher photon energies two such channels are accessible:

$$I_2^- \cdot Ar \rightarrow I^- + I\ (^2P_{3/2}) + Ar \qquad \Delta H_{rxn} = 1.060 \pm 0.006\ \text{eV} \tag{3}$$

$$\rightarrow I^- + I^*\ (^2P_{1/2}) + Ar \qquad \Delta H_{rxn} = 2.003 \pm 0.006\ \text{eV}, \tag{4}$$

where the heats of reaction for channels (3) and (4) are shifted from channels (1) and (2) by the I_2^-–Ar binding energy as determined by Asmis et al. [24] from the photoelectron spectra of I_2^- and $I_2^- \cdot Ar$.

In this Letter, the dissociation of I_2^- and $I_2^- \cdot Ar$ at 413 and 390 nm are presented. Photofragment translational energy distributions for all product channels and three-particle momentum distributions are reported. The results illustrate the capabilities of our instrument with the newly implemented coincidence imaging detector and provide a detailed comparison of these closely related two- and three-body decay processes.

2. Experimental

The ion beam, mass-spectrometer, and laser interaction components of our fast beam photodissociation instrument remain unchanged and have been described in depth previously [4,25,26]; only a brief account is given here. A more detailed description of the new detector is then presented.

Rotationally and vibrationally cooled I_2^- and $I_2^- \cdot Ar$ are produced by flowing argon gas (15 psi) over iodine crystals at room temperature and supersonically expanding the resulting gas mixture through a pulsed piezoelectric valve. A 1 keV electron beam downstream of the valve orifice intersects the free jet expansion. The anions produced in this manner are accelerated to a laboratory beam energy of 8 keV. Ions are mass-selected using a Bakker [27,28] time-of-flight mass spectrometer, which imparts negligible kinetic energy spread to the ion beam, and intersected by the output of an excimer-pumped dye laser with a bandwidth of 0.3 cm^{-1} tuned to a specific photon energy. The photofragments strike an MCP detector assembly with time- and position-sensing (TPS) capabilities for each fragment.

The original TPS detector on this instrument, based on a dual wedge-and-strip anode [4,25], has been replaced by the coincidence imaging detection system shown in Fig. 1. The new system is similar to that designed by Amitay and Zajfman [6] and employed at the CRYRING facility in Stockholm [12]. In this detection scheme, the recoiling photofragments travel past a translatable

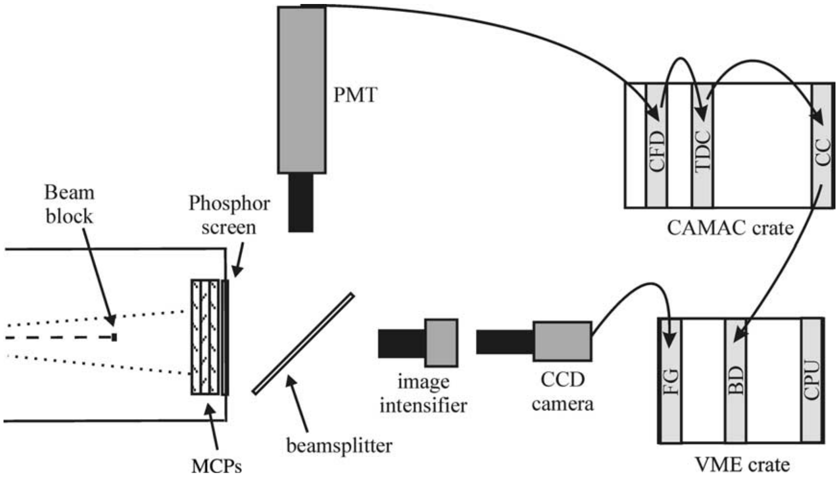

Fig. 1. Schematic diagram of the coincidence imaging detector. The paths of the photofragments and parent ion are represented by dotted and dashed lines, respectively.

5 × 7 mm beam block and collide with an MCP detector coupled to a phosphor screen. Each fragment from a dissociation event produces a spot on the phosphor screen; the positions and arrival times of the fragments are determined by correlated measurements using a charge-coupled device (CCD) camera and a 4 × 4 multi-anode photomultiplier tube (PMT).

In more detail, the front end of the detector consists of three image-quality microchannel plates, 75 mm in diameter, and assembled in a 'Z-Stack'. The front plate of the MCP assembly is held at ground. A high voltage is applied to the last plate which is held at +2.5 kV and pulsed to +3.4 kV during a time period corresponding to the arrival of photofragments. The P20 phosphor screen is held at a constant voltage of +7.5 kV. The entire MCP and phosphor screen detector assembly (BURLE Electro-Optics) is flange-mounted. Emission from the phosphor screen is detected by a CCD camera (Dalsa, CA-D6-0512) via an image intensifier (Photek, MCP140/S20SP43), and by a multi-anode PMT (Hamamatsu, H6568-10). In order to make use of the differing spectral sensitivities of these components, a dichroic beamsplitter (Omega Optical, 565DCLP) with 50% transmission at 565 nm reflects lower wavelengths of light to the PMT and transmits higher wavelengths to the image intensifier and CCD camera. Alternatively, the beamsplitter and image intensifier can be removed, and the PMT positioned off-axis to the phosphor screen, adjacent to the CCD camera. This configuration necessitates the use of higher voltages on the final MCP plate and phosphor screen (+3.8 and +7.7 kV, respectively), resulting in slightly larger spots on the phosphor screen. All data presented in the current investigation were obtained without the beamsplitter or image intensifier.

The position of the impact is obtained from the CCD camera, while the 4 × 4 anode PMT provides timing information and a crude estimate of the position. The output of the CCD camera is digitized by a frame grabber (FG, custom-built at the Weizmann Institute of Science) and read out by a computer (Xycom, XVME-656), both of which are mounted in a VME crate. The 16 individual outputs from the PMT are fed into a constant fraction discriminator (CFD, Lecroy, 3420) to produce fast timing signals that are digitized by a time-to-digital converter (TDC, Phillips Scientific, 7186H); these components are mounted in a CAMAC crate. The VME computer accesses the timing data through the CAMAC branch driver (BD, W-IE-NE-R Plein & Baus GmbH, VC16) and CAMAC crate controller (CC, W-IE-NE-R Plein & Baus GmbH, CC16).

Sample two- and three-body events are presented in Fig. 2. Note that the use of a square 4 × 4

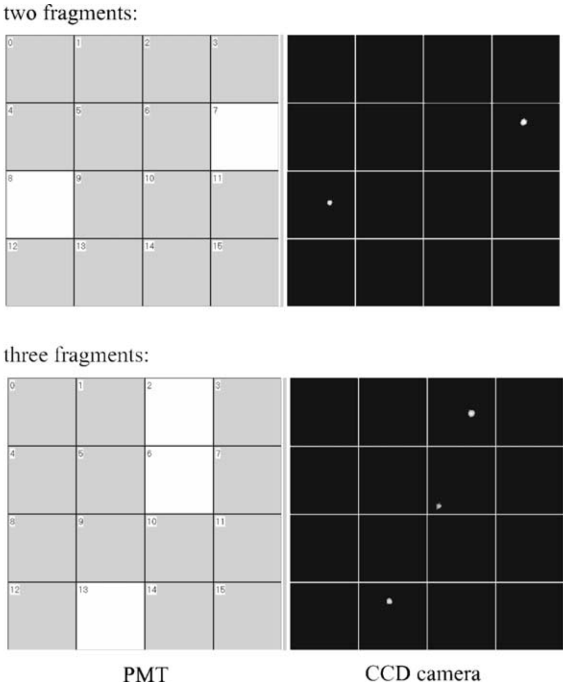

Fig. 2. Sample correlated photodissociation events with two and three fragments. Fragment positions are derived from the CCD camera image and times from the PMT. Active PMT anodes are shown in white.

array minimizes the number of events for which a spot activates more than one PMT anode, compared to previous implementations of this detection system in which an array of 16 adjacent strips was used [6,12]. The entire detection system is pulsed at the same rate as the dissociation laser, 60 Hz, so that information from the both CCD camera and PMT is collected for each laser shot. The time and position of individual fragments are later correlated by comparing the recorded PMT anode to the expected active anode based on the position of the fragment as determined using the CCD camera. Events for which the time and position cannot be correlated or contain more than three or less than two fragments are discarded prior to any further examination.

The analysis for both two- and three-body dissociation follows the methodology outlined by Beckert and Muller [29]. Briefly, given a limited number of product mass channels, each event is matched to the mass channel that minimizes the total momentum in the center-of-mass frame. After determining the masses of the fragments, the velocity vectors of the fragments and center-of-mass position are calculated based on conservation of momentum. Events for which the position of the center-of-mass does not agree with the average position within a user-defined beam radius are discarded as false coincidences. In this manner, we are able to acquire the center-of-mass translational energy release and, for two-body dissociation, the recoil angle of each dissociation event.

The expected resolution from this arrangement is 40 μm in position and 200 ps in time. As the position of a fragment is obtained by calculating the weighted center of a multi-pixel spot, the resolution in position is less dependent on the spot size, and can be determined to within a quarter of a pixel. Based on the photofragment translational energy distribution resulting from the dissociation of O_2 B $^3\Sigma_u^-$ ($v' = 7$), the current translational energy resolution is $\Delta E_T/E_T \approx 0.7\%$, which is comparable to the best resolution obtained with the previous dual wedge-and-strip anode detector [25]. However, for the new detection scheme, this resolution results from the application of one set of calibration parameters to the entire detector, rather than segmenting the detector and employing different parameters for each region as was required previously.

The primary advantage offered by the coincidence imaging detector over the dual wedge-and-strip anode detector is that the latter was limited to the analysis of only two fragments per laser shot. The coincidence imaging scheme allows the direct detection and analysis of multiple fragments, with the restriction that no single PMT anode is activated by more than one phosphor spot. In addition, the diameter of the new detector is larger (75 mm vs 40 mm) and the beam block is considerably smaller (5×7 mm vs 8×40 mm). Consequently, fragments with high and low recoil energies are collected more efficiently, and the maximum photofragment mass ratio for two-body dissociation is higher: 10:1 vs 4:1. Finally, grounding the front plate of the MCP assembly in the current design enables direct detection of anion fragments, in contrast to the previous detector where the front plate was biased at a high negative potential.

3. Results and discussion

3.1. I_2^-

Photofragment translational energy ($P(E_T)$) distributions for I_2^- were obtained at 413 and 390 nm (3.002 and 3.179 eV, respectively), and are shown as solid lines in Fig. 3. Both wavelengths correspond to excitation of the B $^2\Sigma^+_{g,1/2} \leftarrow$ X $^2\Sigma^+_{u,1/2}$ transition, where the upper state is repulsive and correlates to $I^- + I^*$ ($^2P_{1/2}$) products, channel (2). As in the previous studies of bare I_2^- at 395 nm [17,19], this is the only observed channel. The width of the features in the distributions reflects the internal excitation of the parent ion. Using the rotational and vibrational constants of I_2^- to fit these features yields a parent temperature of 100–120 K. From the fragment kinetic energy release and spin–orbit splitting of the iodine atom, the dissociation energy, D_0, is given by:

$$D_0 = E_{h\nu} + E_{\text{int}}(I_2^-) - E_T - E_{\text{elec}}(I), \tag{5}$$

where E_T at zero parent internal excitation is taken as halfway up the steep rising edge of the $P(E_T)$ distribution (dashed vertical lines in Fig. 3). An average value of $D_0 = 1.012 \pm 0.008$ eV is obtained which is in reasonable agreement with the previously determined value of 1.007 ± 0.005 eV by Zanni et al. [16]. Additionally, analysis of the photofragment angular distributions yields an anisotropy parameter [30] of $\beta = 1.8 \pm 0.1$. This measurement is consistent with prompt dissociation following excitation of the parallel B $\leftarrow$ X transition.

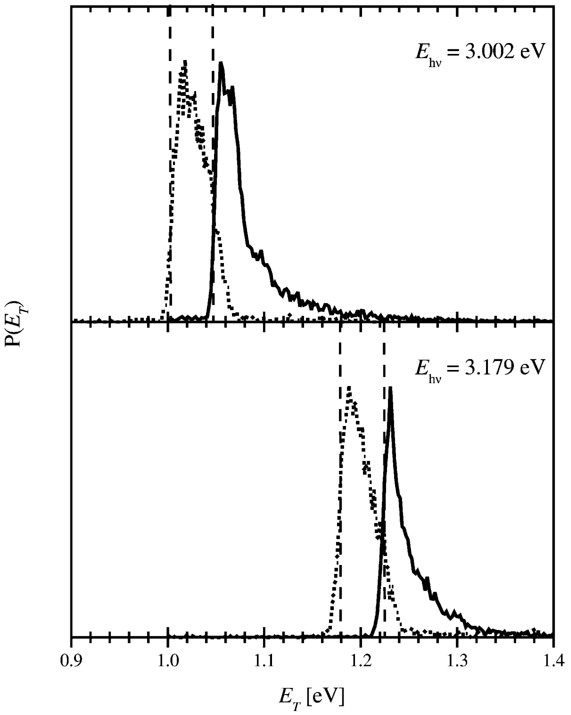

Fig. 3. Photofragment translational energy distributions resulting from excitation of the B $^2\Sigma^+_{g,1/2} \leftarrow$ X $^2\Sigma^+_{u,1/2}$ transition of I_2^- (solid) and three-body dissociation of $I_2^- \cdot Ar$ (dotted). The vertical dashed lines indicate the maximum kinetic energy release for I_2^- and $I_2^- \cdot Ar$ based on the I_2^- dissociation energy and I_2^-–Ar binding energy as determined in the current work.

3.2. $I_2^- \cdot Ar$

The photodissociation of $I_2^- \cdot Ar$ at 413 and 390 nm was also investigated. Images resulting from valid coincident events in which two and three fragments were observed are presented in the left and right panels, respectively, of Fig. 4. The laser polarization is vertical in the plane of the figure in all of the images. The photoproduct masses are found to be equal for the two-body events; therefore, the two-fragment images arise solely from events in which the iodine fragments are detected and the Ar atom either strikes the beam block or is not detected owing to less than unit efficiency. Similar events were seen in our previous studies of the photodissociation of I_3^- and I_3 [31,32]. In the three-fragment images, the Ar atoms have sufficient translational energy to travel past the beam block and appear as a bright spot in the center of the image. Thus, all of the observed valid events are attributed to three-body dissociation, in which either all three photoproducts are observed (30–33%) or the Ar atom goes undetected (70–67%).

$P(E_T)$ distributions for the three-body events (i.e., those for which all three fragments were detected) are shown as dotted lines in Fig. 3. These distributions are similar to those obtained for I_2^- dissociation at the same wavelengths, indicating that they correspond to channel (4) with no quenching of the I^* ($^2P_{1/2}$) fragment by the Ar atom, but are shifted to lower translational energy

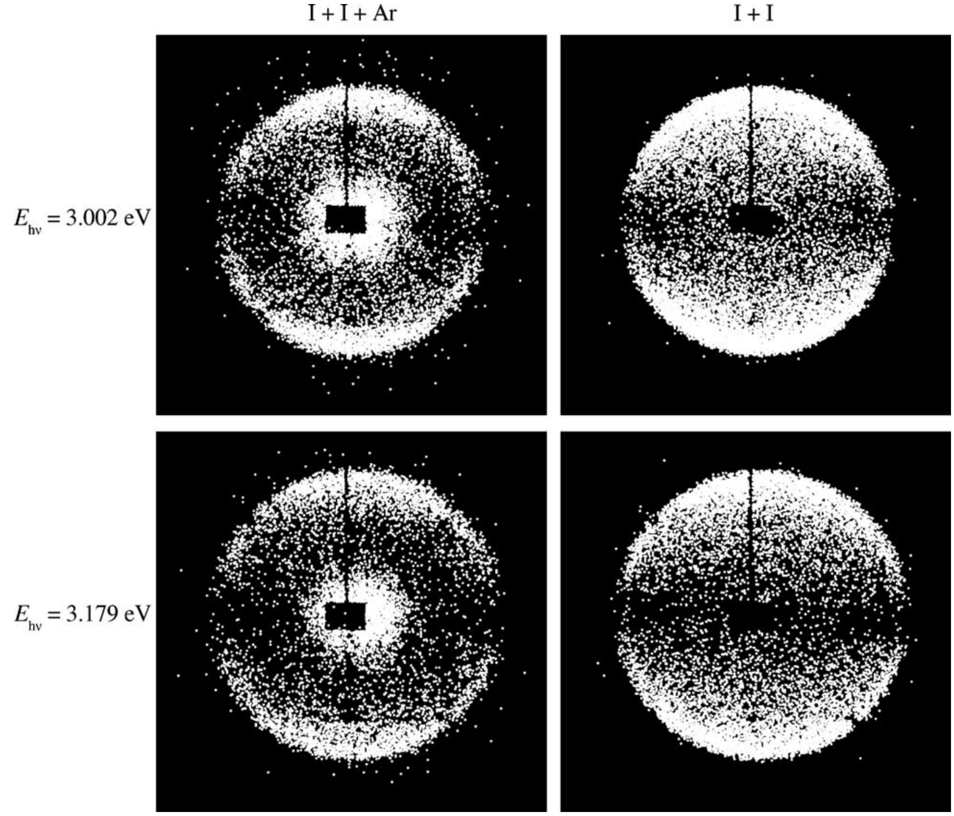

Fig. 4. Images of fragment positions for the I + I + Ar and I + I mass channels obtained with vertical laser polarization. Points on the image correspond to the center of a fragment spot on the detector.

by an average value of 45 ± 8 meV. This shift corresponds to the I_2^-–Ar binding energy. The previously determined binding energy of 53 ± 4 meV by Asmis et al. [24] lies within the error bars of the current measurement. One other point of comparison is that the 'tail' extending to higher E_T in the I_2^- $P(E_T)$ distributions is not present in the $I_2^- \cdot$ Ar distributions because clusters in which the I_2^- internal energy is greater than the binding energy dissociate before arriving at the laser interaction region. The translational energy distributions of the two-body events are less relevant, since they do not include the small but unknown contribution from the Ar atom. However, examination of the photofragment angular distributions for the two-body events yields an anisotropy parameter [30] of $\beta = 1.7 \pm 0.1$, similar to that seen for bare I_2^-.

The three-body coincidence measurements yield additional insight into the nature of the dissociation dynamics. In Fig. 4, the concentration of the Ar signal around the center of the detector indicates that the Ar atom is receiving a small fraction of the total momentum. This is seen in more detail in the Dalitz plots [7,13,33] for the three-body events, Fig. 5, which show the momentum partitioning among the fragments for each dissociation event. The line AB corresponds to events in which the iodine fragments have equal, but opposite momenta, with point A indicating events with zero momentum in the Ar atom. The intensity in the plots is focused in the region with low Ar momentum, but rather than peaking on line AB, extends above and below line AB, thereby denoting unequal momenta for the iodine fragments.

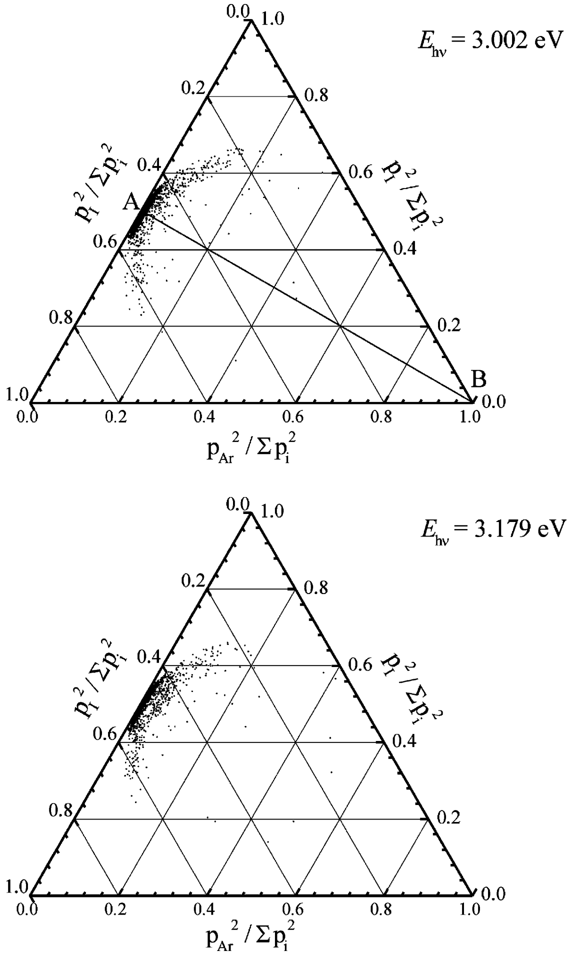

Fig. 5. Dalitz plots of momentum partitioning among the fragments in the three-body dissociation of $I_2^- \cdot Ar$ to $I^- + I^*$ $(^2P_{1/2}) + Ar$. Line AB denotes configurations with equal momentum in the iodine fragments. As the iodine anion and neutral are indistinguishable in the current experiments, the iodine fragment axes represent a combination of both neutral and charged species.

$I_2^- \cdot Ar$ is calculated to have a C_{2v}, T-shaped equilibrium geometry [34,35], with the Ar atom lying in the plane bisecting the I–I bond. We are exciting a repulsive electronic state of the I_2^- and therefore expect the initial dynamics to involve extension of the I–I bond. If synchronous concerted dissociation were to occur from the T-shaped geometry, with all bonds breaking simultaneously, then one would expect most of the intensity in the Dalitz plots along the line AB [13], in contrast to the results in Fig. 5. On the other hand, a two-step mechanism along the lines of:

$$I_2^- \cdot Ar \rightarrow I + I^- \cdot Ar \rightarrow I + I^- + Ar, \qquad (6)$$

with the Ar atom associating itself, however briefly, with the charged atomic fragment, is difficult to reconcile with very low momentum of the Ar atom. Our observations likely reflect the fact that the Ar atom is quite weakly bound to the I_2^- and consequently has substantial zero-point amplitude. Thus, the starting point for dissociation is more typically a geometry with the Ar atom asymmetrically placed with respect to the two I atoms rather than the C_{2v} equilibrium structure. This leads to unequal partitioning of momentum between the two I atoms even if there is near-simultaneous breaking of all bonds.

4. Conclusions

The photodissociation of I_2^- and $I_2^- \cdot Ar$ was investigated at 413 and 390 nm with a coincidence imaging detector that has recently been coupled to our fast beam photofragment translational spectrometer. Results from this study demonstrate the utility of this method for the study of two- and three-body dissociation as well as the extension of our capabilities to the direct detection of anionic fragments. Our results on the three-body dissociation of $I_2^- \cdot Ar$ show that the Ar momentum is typically very low and the two I atoms generally have unequal momenta, implying a near-simultaneous breaking of all bonds but reflecting contributions from asymmetric initial nuclear configurations to the dissociation dynamics.

Acknowledgements

This research is supported by the Director, Office of Basic Energy Sciences, Chemical Sciences Division of the U.S. Department of Energy under Contract No. DE AC03-76SF00098. The authors would like to thank Dr. Daniel Zajfman of the Weizmann Institute of Science for his assistance in the implementation of our coincidence imaging detector. K.E.K. is a National Science Foundation predoctoral fellow.

References

[1] R.E. Continetti, Annu. Rev. Phys. Chem. 52 (2001) 165.

[2] D.P. de Bruijn, J. Los, Rev. Sci. Instrum. 53 (1982) 1020.

[3] H. Helm, P.C. Cosby, J. Chem. Phys. 86 (1987) 6813.

[4] R.E. Continetti, D.R. Cyr, D.L. Osborn, D.J. Leahy, D.M. Neumark, J. Chem. Phys. 99 (1993) 2616.

[5] P. Jukes, A. Buxey, A.B. Jones, A.J. Stace, J. Chem. Phys. 109 (1998) 5803.

[6] Z. Amitay, D. Zajfman, Rev. Sci. Instrum. 68 (1997) 1387.

[7] L.M. Wiese, O. Yenen, B. Thaden, D.H. Jaecks, Phys. Rev. Lett. 79 (1997) 4982.

[8] K.A. Hanold, A.K. Luong, R.E. Continetti, J. Chem. Phys. 109 (1998) 9215.

[9] B. Farizon, M. Farizon, M.J. Gaillard, F. Gobet, M. Carre, J.P. Buchet, P. Scheier, T.D. Mark, Phys. Rev. Lett. 81 (1998) 4108.

[10] U. Muller, T. Eckert, M. Braun, H. Helm, Phys. Rev. Lett. 83 (1999) 2718.

[11] M. Barat, J.C. Brenot, H. Dunet, J.A. Fayeton, Y.J. Picard, J. Chem. Phys. 113 (2000) 1061.

[12] S. Datz, R. Thomas, S. Rosen, M. Larsson, A.M. Derkatch, F. Hellberg, W. van der Zande, Phys. Rev. Lett. 85 (2000) 5555.

[13] C. Maul, K.H. Gericke, J. Phys. Chem. 104 (2000) 2531.

[14] R. Parson, J. Faeder, N. Delaney, J. Phys. Chem. 104 (2000) 9653.

[15] B.J. Greenblatt, M.T. Zanni, D.M. Neumark, Chem. Phys. Lett. 258 (1996) 523.

[16] M.T. Zanni, T.R. Taylor, B.J. Greenblatt, B. Soep, D.M. Neumark, J. Chem. Phys. 107 (1997) 7613.

[17] S. Nandi, A. Sanov, N. Delaney, J. Faeder, R. Parson, W.C. Lineberger, J. Phys. Chem. 102 (1998) 8827.

[18] M.T. Zanni, V.S. Batista, B.J. Greenblatt, W.H. Miller, D.M. Neumark, J. Chem. Phys. 110 (1999) 3748.

[19] A. Sanov, T. Sanford, S. Nandi, W.C. Lineberger, J. Chem. Phys. 111 (1999) 664.

[20] M.T. Zanni, A.V. Davis, C. Frischkorn, M. Elhanine, D.M. Neumark, J. Chem. Phys. 112 (2000) 8847.

[21] E.C.M. Chen, W.E. Wentworth, J. Phys. Chem. 89 (1985) 4099.

[22] P.E. Maslen, J. Faeder, R. Parson, Chem. Phys. Lett. 263 (1996) 63.

[23] V. Vorsa, P.J. Campagnola, S. Nandi, M. Larsson, W.C. Lineberger, J. Chem. Phys. 105 (1996) 2298.

[24] K.R. Asmis, T.R. Taylor, C.S. Xu, D.M. Neumark, J. Chem. Phys. 109 (1998) 4389.

[25] D.J. Leahy, D.L. Osborn, D.R. Cyr, D.M. Neumark, J. Chem. Phys. 103 (1995) 2495.

[26] D.L. Osborn, H. Choi, D.H. Mordaunt, R.T. Bise, D.M. Neumark, C.M. Rohlfing, J. Chem. Phys. 106 (1997) 3049.

[27] J.M.B. Bakker, J. Phys. E Sci. Instrum. 6 (1973) 785.

[28] J.M.B. Bakker, J. Phys. E Sci. Instrum. 7 (1974) 364.

[29] M. Beckert, U. Muller, Eur. Phys. J. D 12 (2000) 303.

[30] R.N. Zare, Mol. Photochem. 4 (1972) 1.

[31] H. Choi, R.T. Bise, A.A. Hoops, D.M. Neumark, J. Chem. Phys. 113 (2000) 2255.

[32] H. Choi, T.R. Taylor, R.T. Bise, A.A. Hoops, D.M. Neumark, J. Chem. Phys. 113 (2000) 8608.

[33] R.H. Dalitz, Philos. Mag. 44 (1953) 1068.

[34] V.S. Batista, D.F. Coker, J. Chem. Phys. 110 (1999) 6583.

[35] J. Faeder, R. Parson, J. Chem. Phys. 108 (1998) 3909.